



ELSEVIER

Contents lists available at ScienceDirect

Mechatronics

journal homepage: www.elsevier.com/locate/mechatronics

Novel wireless sensing platform for experimental mapping and validation of ship air wake[☆]



Anil Kumar, Pinhas Ben-Tzvi*

Department of Mechanical Engineering, Virginia Tech, Blacksburg, VA 24060, USA

ARTICLE INFO

Keywords:

Ship air wake
Particle swarm optimization
Neural networks
RC helicopter dynamics
Wind turbulence

ABSTRACT

This paper presents the mechatronic design and analysis of a wireless sensing platform developed for the experimental mapping and validation of the air wakes generated by cruising naval vessels. The presented sensing system uses an RC helicopter as its carrier platform and uses the helicopter's dynamics for spatial 3D mapping of wind turbulence. In this paper, the proposed telemetry system models the dynamic response of the helicopter to pilot inputs under artificially generated wind conditions and then uses neural network based models to estimate the air wake distribution. The telemetry system uses a wireless sensor network comprising of sensors such as an Inertial Measurement Unit (IMU), optical trackers, and GPS to measure the dynamics of a flying RC helicopter. The system was trained and calibrated in a climate controlled indoor environment with artificially generated wind conditions. This paper focuses on both hardware and software aspects of the latest iteration of the telemetry system (version 3.0). The presented telemetry system is also tested with a modified YP676 naval training vessel in the Chesapeake Bay area, under a wide range of wind conditions and the results were compared against CFD simulations.

1. Introduction

The operation of helicopters on naval vessels is a very risky and challenging task due to ship air wakes and limited flight deck area. Ship air wake is a trail of air turbulence generated in the lee of the superstructure of a cruising naval vessel. To minimize these operational risks, 'safe launch and recovery envelopes' are prescribed for operating helicopters with each class of naval vessel in order to avoid high air wake zones during take-off and landing [1]. Such safe flight envelopes are often determined with Computational Fluid Dynamics (CFD) models and/or manual flight testing. Because of the serious naval safety implications of ship air wakes, many navies around the globe have ship air wake study programs [2–4]. Significant research has been done to develop high-fidelity CFD models to predict air wake patterns [3,5] and interactions with rotary wing aircraft [6–11]. However, existing CFD models need extensive experimental data for validation. Manual flight testing, on the other hand, is not only risky but also highly subjective as it depends on the pilot's response. Thus, there is a need for an instrumentation system capable of measuring ship air wake intensities in a non-subjective manner. To obtain experimental ship air wake data, most researchers have pursued either wind tunnel testing or relied on in-situ wind velocity measurements using anemometers.

1.1. Wind tunnel testing

Wind tunnel testing has been the preliminary and most common source for ship air measurement in the naval science community. Such studies often use a scaled-down model of naval vessels in wind tunnel and measure wind flow field. These types of setups have used a variety of sensing modalities including laser Doppler anemometry [12], hot wire based Omniprobe anemometry [3,9] and Particle Image Velocimetry [2,10,13]. In a similar study, Kääriä et al. immersed a model helicopter in a water tunnel to validate the aerodynamic interactions of a helicopter with ship air wakes [11]. The transducers used in these measurements are very sensitive and expensive, so they can safely be operated only in controlled environments like wind tunnels. The wind tunnel testing does provide significant insight into wind flow in ship air wake zones, but lacks fine details in flow pattern due to scaling issues. Additionally, both the model holder and the walls of wind tunnel affect the readings, and their effects must be accounted for in the experimentation.

1.2. In-situ measurements

Use of anemometers is the most common means for in-situ wind

[☆] This paper was recommended for publication by Associate Editor Prof. Hamid Reza Karimi.

* Corresponding author.

E-mail address: bentzvi@vt.edu (P. Ben-Tzvi).

2.1. Pilot inputs

The rotor hub of the helicopter controls the pitch angle of the rotor blades by making use of a swash plate mechanism. The pilot's inputs for the rotor hub are composed of three elements viz. Collective (θ_0), Roll Cyclic (θ_c) and Pitch Cyclic (θ_s). The collective input results in an offset in the rotor pitch angles and is responsible for the overall hovering thrust generated by the helicopter. The cyclic input on the other hand makes the rotor pitch change cyclically with the rotor position and hence is responsible for thrust vectoring (tilting) and other desired maneuvering. In simplified form, the rotor pitch angle can be represented as follows in terms of collective and cyclic inputs and rotor position:

$$\theta(\psi) = \theta_0 + \theta_c \cos(\psi) + \theta_s \sin(\psi). \quad (3)$$

2.2. Aerodynamic loading and helicopter dynamics

To estimate the aerodynamic loading on the main rotor blades, it can be assumed that the blades are composed of infinitesimally thin airfoil sections of chord length c and thickness dr_b (Fig. 1B). Wind vector experienced by any thin airfoil section depends on three parameters: rotor speed, fuselage rotation (rate), and local wind conditions (comprising of both rotor induced wakes and external wind turbulence). Because of near hover operation, the effect of relative wind due to translational motion can be ignored. At any point in time, the relative wind velocity vector experienced by a rotor blade due to its motion alone can be expressed in terms of rotor speed and angular rates as follows:

$$u_{bh}(r_b, \psi) = [-r_b \Omega s \psi \quad r_b \Omega c \psi \quad -qr_b c \psi + pr_b s \psi]^T. \quad (4)$$

Here, u_{bh} is the wind velocity vector relative to the helicopter blade (airfoil) element at a radial distance of r_b and angular location ψ in the helicopter's frame of reference (while rotating at speed Ω) and $\{p, q, r\}$ constitute the three angular rates of the helicopter fuselage. Additionally, the effect of yaw rate r is ignored here as $r < \Omega$. By subtracting (4) from external wind conditions, and pre-multiplying with the rotation matrix corresponding to the rotor position, the net wind experienced by the helicopter blade in element in the blade's frame of reference can be written as follows:

$$u_{wb}(r_b, \psi) = \begin{bmatrix} u_x \\ u_y \\ u_z \end{bmatrix}_{wb} = R_b^h \left(\begin{bmatrix} u_x \\ u_y \\ u_z \end{bmatrix}_{wh} + \begin{bmatrix} 0 \\ 0 \\ v \end{bmatrix}_{ih} - \begin{bmatrix} u_x \\ u_y \\ u_z \end{bmatrix}_{bh} \right). \quad (5)$$

Here u_{wb} is the net wind velocity vector relative to the helicopter blade (airfoil) element in the blade's frame of reference, R_b^h is the rotation matrix arising from rotor position ψ to convert wind estimates relative to blade elements from rotor hub to blade's frame of reference. The quantity $\{u_x, u_y, u_z\}_{wh}^T$ in (5) represents the external wind vector (spatially varying) in helicopter's frame of reference and v is helicopter induced rotor inflow (in helicopter's frame of reference) which depends on helicopter's mode of operation. For near hover conditions, the rotor inflow can be assumed to be uniform over the rotor disk area [25]. Since the radial component of the wind does not contribute towards the thrust generation, only the $\{u_y, u_z\}_{wb}$ components contributed towards the blade aerodynamics. The aerodynamic loads generated by the rotor blade depend on the wind's 'angle of attack' of the relative with respect to the blade comprising of blade pitch angle θ , wind incidence angle ϕ . So, by substituting (5) in (1) and (2), the differential lift dl generated by an element can be expressed as follows:

$$dl(r_b, \psi) = 1/2\rho(r_b\Omega)^2 c a_0 (\theta - \phi) dr_b; \quad \begin{cases} \phi(r_b, \psi) = \tan^{-1}(u_z/u_y) \approx u_z/u_y \\ \{u_y, u_z\} = \{u_y, u_z\}_{wb} \end{cases} \quad (6)$$

These aerodynamic loads, when integrated over the length of the

rotor blades, result in a net force and moment on helicopter. The proposed telemetry system focuses on the rotational effects of wind turbulence on the helicopter and thus only the moments $\{L, M, N\}$ acting on the helicopter are studied. Rigid body equations of rotational motion for a helicopter are given by the Newton-Euler equations shown below (7).

$$\begin{aligned} I_{xx} \dot{p} &= qr(I_{yy} - I_{zz}) + (L_{mr} + L_g) \\ I_{yy} \dot{q} &= rp(I_{zz} - I_{xx}) + (M_{mr} + M_g) \\ I_{zz} \dot{r} &= pq(I_{xx} - I_{yy}) + (-N_{mr} + N_{tr}) \end{aligned} \quad (7)$$

Here, $\{I_{xx}, I_{yy}, I_{zz}\}$ are the three moments of inertia of the helicopter respectively around X (right fin), Y (nose) and Z (up) axis. The subscripts mr , tr and g in the moment terms represent 'main rotor', 'tail rotor' and 'gravity', respectively. It is worth noting that the effect of the non-diagonal component (predominately I_{xz}) of the inertia has been neglected here as the values range from 7 to 30 times smaller than the diagonal entries.

The differential lift generated by the pilot controlled rotor pitch and wind flow pattern are the main and most prominent reason behind the helicopter's rotational dynamics. The differential lift (6), when multiplied with the radial distance from the rotor, can be integrated over the rotor length and position to obtain the net moment generated by one rotor blade (T) and should be multiplied by the number of blades (N_b) to obtain net rotor moment. The Pitch and Roll moment [25] from the main rotor can be obtained as follows.

$$\begin{aligned} L_{mr} &= N_b/2\pi \int_{\psi=0}^{2\pi} T(\psi) \sin \psi d\psi; \quad M_{mr} = -N_b/2\pi \int_{\psi=0}^{2\pi} T(\psi) \cos \psi d\psi; \\ T(\psi) &= 1/2C_A \rho \Omega^2 c \int_{r_b=0}^R r_b^3 (\theta(\psi) - \phi(\psi, r_b)) dr_b \end{aligned} \quad (8)$$

Here, the main rotor's yaw moment is ignored primarily because the pitch and roll moments are the more critical quantities from a naval safety perspective. In addition to this, the heading control system of the RC helicopter compensates for any aerodynamic disturbances along yaw axis through tail rotor. In the moment equations of the helicopter (7, 8), other than the moments due to the gravity (L_g and M_g), all the moments depend on pilot inputs and wind conditions. The orientation of the helicopter along the pitch and roll axes create a 'pendulum type' restoring torque (9) which depends on the pitch and roll attitude angles of the helicopter.

$$L_g = -rm_A g \sin(\theta); \quad M_g = -rm_A g \sin(\phi). \quad (9)$$

Here, r is the location of the center of mass with respect to the rotor hub. Fig. 2 shows the general impact of aerodynamic thrust and attitude on angular rates changes (moment) of the helicopter. In addition, g is acceleration due to gravity and m_A is the mass of the helicopter. The angular accelerations (7) of the helicopter can be written in terms of gravity and aerodynamic moments, which are non-linear functions of previous angular rates, air conditions, pilot inputs and helicopter attitude.

$$\begin{aligned} \dot{p}_t &= f(p_{t-1}, q_{t-1}, r_{t-1}, L_g(\theta), L_{mr}(\mathbf{P}, \mathbf{W})) \\ \dot{q}_t &= g(p_{t-1}, q_{t-1}, r_{t-1}, M_g(\phi), M_{mr}(\mathbf{P}, \mathbf{W})) \end{aligned} \quad (10)$$

Here, \mathbf{P} and \mathbf{W} correspond to the set of pilot servo actuator inputs and wind model parameters, respectively. The nonlinear functions f, g and the main rotor moment estimates, being too complicated to be solved analytically, are determined experimentally using machine learning algorithms. It is worth noting that the dynamics arising from the rotor blade flapping have been ignored in this analysis. The rotor blade flapping manifests itself as high-frequency fluctuations in the helicopter's angular acceleration measurement. It may be removed by applying a suitable low pass filter to the IMU reading. In addition, the net aerodynamic load on the rotor blades is an arithmetic sum of the

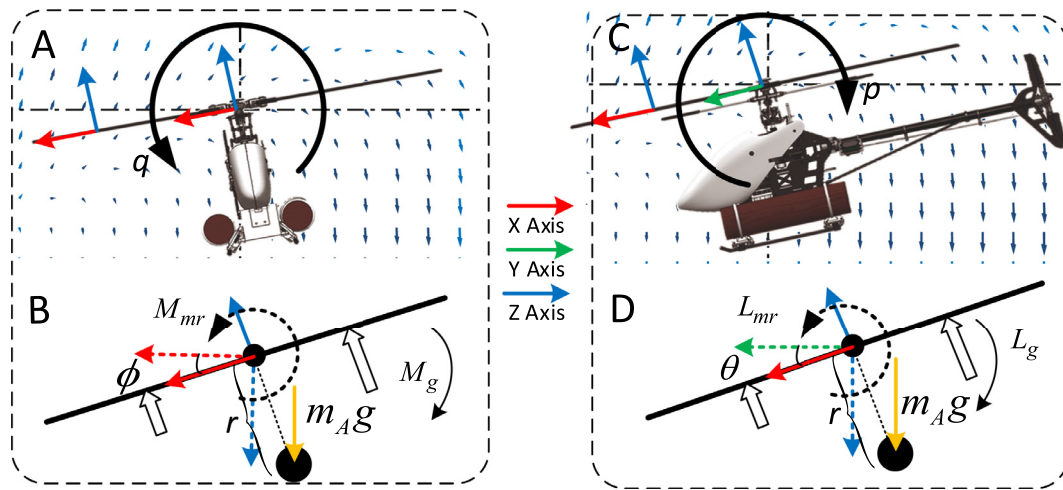


Fig. 2. Factors affecting helicopter dynamics (angular rates): (A),(B) Roll Dynamics, (C),(D) Pitch Dynamics.

components viz. pilot inputs and wind conditions. Since pilot inputs, helicopter attitude, and previous angular rates can be measured and their aerodynamic loads can be modeled, any deviation in the measured angular acceleration from the estimated values is essentially the result of wind disturbances and can be correlated to ship air wakes. Ship air wake turbulence is the most predominant source of deviations.

3. Telemetry system hardware

The proposed telemetry system comprises of two independent instrumentation sub-systems called the rover module and the base module. Fig. 3 shows the prototypes of both modules.

These modules communicate with each other via a 3.5 Mbps long-range Wi-Fi network with an update rate of up to 150 Hz (~5 times the rotor speed). The Wi-Fi router uses two types of antennas, one is an omnidirectional short-range rod antenna and the other is a long-range directional Yagi antenna. In tandem, both antennas provide a long-range network coverage without any data loss. To estimate the ship air wake patterns, an RC helicopter retrofitted with the rover module is flown in the target area. The rover module then sends the helicopter's dynamics data to the base module over the Wi-Fi network. A computer connected to the base module records and processes the data then displays appropriate results/flight parameters on the screen in the form of graphs and trajectories. Both modules in the proposed wireless telemetry system use aviation grade INS/IMU sensors to measure the position and dynamics of the helicopter and the boat at a high rate (up to 800 Hz).

3.1. Rover module

The rover module is a battery powered instrumentation board that reads data from a VN200 INS development board (under the green interface board in Fig. 3A) and Piksi RTK, and sends the positioning data via XBee Wi-Fi module. The central processing unit of the rover module is an ARM Cortex M4 microcontroller that offers three UART serial ports. Fig. 4A shows the electrical schematics of the rover module. One serial port is being used to connect the RTK to the system, while the second one is used to interface the Wi-Fi module. The third serial port is left unused for future upgrades. The rover module acquires helicopter flight parameters such as position, attitude, speed, angular rates, and acceleration IMU packets with an update rate of 150 Hz through the VN200 over SPI serial link.

The XBee modules with an omni-directional antenna had limited transmission/reception capability in open areas, the telemetry and thus required a custom RF communication system. Since the omnidirectional rod antennas have a cylindrical radiation pattern, two perpendicular 2.4 GHz rod antennas are used on the rover module to achieve transmission in all directions (Fig. 3A). To further improve the communication range and network reliability, a 2 W 2.4 GHz RF amplifier was used with the XBee Wi-Fi transceivers.

3.2. Base module

The base module is an instrumentation board that receives pilot inputs (from a radio controller) and data from the rover module. Fig. 3B shows the assembly of the base module on a 3D printed mount, which

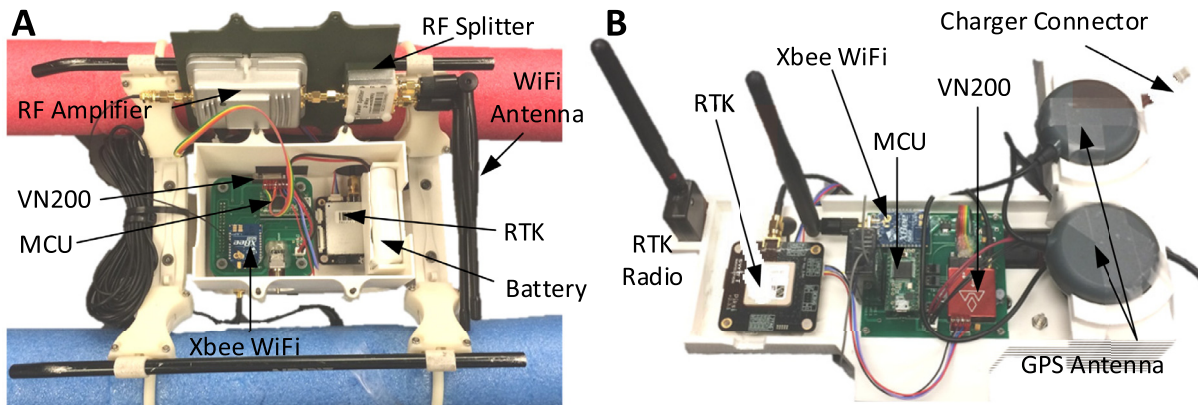


Fig. 3. Telemetry system hardware setup: (A) Rover module (Bottom view with cover removed); (B) Base module (Rearview without cover).

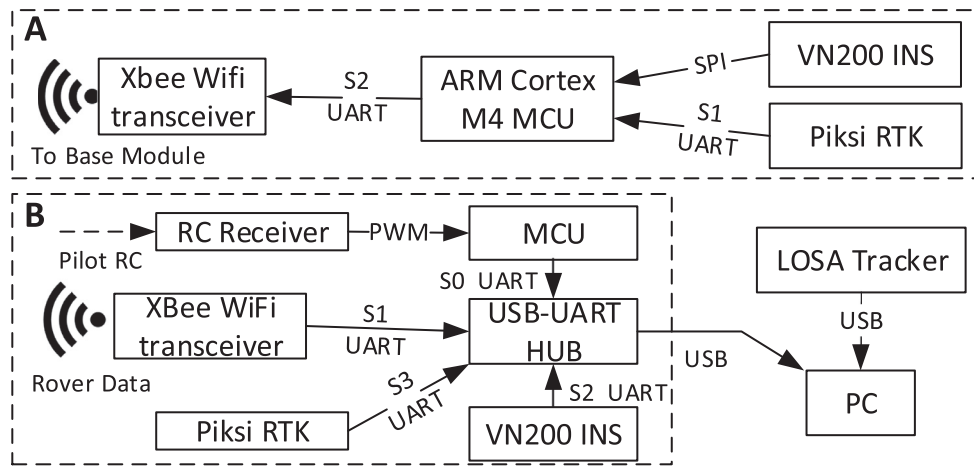


Fig. 4. Electrical schematics of: (A) Rover module, and (B) Base module.

helps it fit rigidly on the ship during experiments. The core of this module is a USB to a quad-UART hub that connects up to four serial devices to a computer via USB port. An ARM Cortex M4 MCU board reads five channels of PWM inputs from an RC receiver and sends the pilot inputs to the PC via one of the serial ports on the hub.

Data from the rover module is received by the Xbee Wi-Fi wirelessly and directly sent to the PC via serial port. Similarly, INS data from the VN200 sensor is sent to the PC via Serial port (S2). The fourth serial port (S3) is used (via a 4 pin connector) to interface the Piksi RTK to the system. The RTK system on the base module works in ‘base mode’ and sends the RTK correction data to the RTK on the rover module through a radio link. The baseline solution for the relative position is estimated on the RTK in the rover module and sent to the base module over the Wi-Fi link. Fig. 4B shows the electrical schematics of the ship base module.

During measurement, the proposed telemetry system is mounted on a T-REX 600E PRO RC helicopter and flown in the lee of the superstructure of YP676 in a sweeping trajectory. The data is received on the base computer connected to the base modules using a custom-made GUI software in NI® LabVIEW™. The GUI allows the user to acquire and record data in real-time without running into buffering issues due to its highly optimized serial virtual COM port and carefully programmed multi-threaded data handling capabilities. The GUI interfaces with the COM ports emulated by the base module and LOSA tracker [26] (a custom-made patent pending motion tracking device) to synchronize the data according to the associated time-stamps and store the data in text files for post processing. The relative position of the helicopter in the boat’s frame of reference is obtained from the position and heading estimates from LOSA tracker/VN200 INS (on both modules).

4. System training

As shown in section II, the helicopter’s moment measurements (angular acceleration) can be split into three components viz. a gravity component, the cross product of the inertia component, and the main rotor component (comprising of effects of local wind conditions and pilot inputs). Although the ship air wakes have both rotational and translational impacts (in all three axes) on helicopters, pitch and roll tilting are the most critical effects from a naval safety perspective. This paper thus focuses on modeling the pitch and roll dynamics of the RC helicopter to extract wind turbulence conditions. Data for training the system to learn the helicopter’s dynamics as a function of pilot inputs and state variables was collected by flying the instrumented helicopter in large indoor facilities. The helicopter was flown at an altitude of more than two rotor diameters (~ 2.5 m, to eliminate any rotor-ground effect) to perform a variety of high dynamics maneuvers and oscillatory

tilting motion (at varying frequency) to create a versatile database of pilot input combinations and corresponding angular acceleration measurements.

4.1. Feed forward network

The proposed system uses a feedforward neural network to model the dynamics of the helicopter in absence of external disturbance (ship air wakes). Neural networks are interconnected directed graphs (Fig. 5) comprising of cascaded MISO nodes known as neurons [27].

The proposed network used a ‘hyperbolic tangent’ sigmoid function and a ‘purelin’ linear transfer function as objective functions for the neurons in hidden layer and output layer respectively. As shown in (10), the helicopter’s angular acceleration measurements depend on seven inputs viz. three channels of angular rate readings, tilting angle (roll/pitch) and three swash plate pilot inputs. Thus, the input layer for the network consisted of 7 neurons. In addition, two separate hidden-layered feedforward networks were used for modeling the helicopter’s angular acceleration along pitch and roll axis, the output layer consisted of a single neuron. For a network (Fig. 5) with $\{M, N\}$ being the number of neurons in the hidden layers, the total number of variables to be optimized is $(7 \times M + M \times N + N \times 1)$ weights and $(M + N + 1)$ biases.

4.2. Particle swarm optimization

Backpropagation neural networks rely on gradient descent methods for training, which can converge at local error minima in training weight space. To overcome this limitation, the proposed system uses a particle swarm optimization (PSO) [28,29] technique with 10-fold cross validation for training the neural network. PSO is a non-gradient stochastic sampling based optimization technique mimicking swarm intelligence of bird flocks with mathematical models.

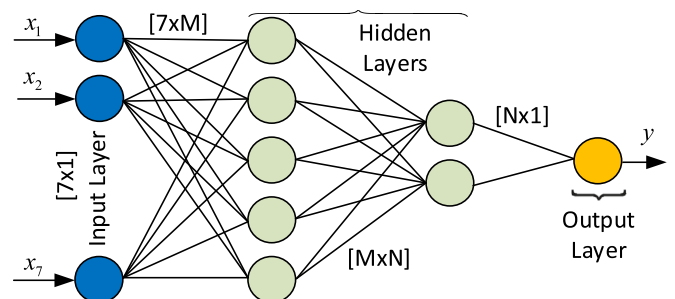


Fig. 5. Proposed network topology.

PSO is typically used for global optimization in multidimensional search space where traditional neural networks are susceptible to converging at local extrema. Each particle involved in PSO is defined by a multidimensional vector in the search space with random initialization. In addition to this, all the particles retain a memory of their individual best performance and the global best performance (among all particles) over that course of training. With each iteration, the particles are evaluated according to their applications and the individual and global best particles are updated. In a swarm with X_{ib} and X_{gb} being individual particle's best performance and the global best particle respectively, the particle velocities (V) and position (X) for any particle are updated as follows:

$$X_N = X_{N-1} + V_N |V_N = mV_{N-1} + C_1 r_1 (X_{ib} - X_{N-1}) + C_2 r_2 (X_{gb} - X_{N-1}). \quad (11)$$

Here, m (0.2) is the inertia coefficient, C_1 , C_2 (0.1, 0.2, respectively) are exploitation coefficients and r_1 , r_2 are exploration coefficient (random numbers generated between 0 and 1). This process continues until the global best particle settles at the optimum position.

4.3. Training neural networks using PSO

The offline network training was done using custom-made MATLAB scripts, which not only performed data preprocessing, but also emulated neural network models by extracting weights and biases from individual particles in the swarm. To train the neural networks using PSO, a swarm of 5000 particles was randomly initialized, with the dimensionality of each particle decided by the topology of the network under consideration. The networks were trained multiple times (with different topology each time) with the number of neurons varied between 6 and 3 in both hidden layers. It was found that the networks with hidden layer topologies of {5,2} and {4,3} for roll and pitch acceleration prediction outperformed all other network topologies. All the particles in the swarm were initialized using random weights/biases. To keep the biases within the reach of the randomly assigned particles, the input vectors to the network models were normalized to zero mean and unit standard deviation. The global and individually best-performing particles were updated on the basis root mean squared error on the training data.

As mentioned before, 10-fold cross-validation was used for retrieving the optimum network during the training process. Ten percent of the training data was used for cross-validation and the network was said to be trained when the change in the prediction error was less than (0.01 rad/s²) and the prediction error on the cross-validation data is lesser than or equal to that of the training data. The network was trained on 30,800 training samples (~30% data) and tested on separate 73,100 samples (~70% data). Fig. 6 shows the progression of the

training progress.

The mean absolute prediction error on the testing data set was found to be 0.2868 rad/s² and 0.2441 rad/s² for the roll pitch acceleration prediction network respectively. Fig. 7 shows the angular acceleration prediction error on a sample test flight for the both networks. Fig. 7 also presents the prediction error distribution for the two networks in the form of histogram plots.

5. Indoor validation experiment

To test the capability of the telemetry system, the helicopter was flown in a wind controlled indoor environment. To generate artificial turbulent wind conditions, a setup of two 24-in diameter fans placed opposite to each other was implemented (Fig. 8). The wind flow between the two fans was measured by using a three-axis Young™ Ultrasonic Anemometer (Model 81,000) [30] mounted on a pole with adjustable height. The LOSA 3D motion tracking system [26] was used to transfer the wind measurements from the sensor's frame of reference to the global (wind source) frame of reference. The active marker for the LOSA tracker was rigidly mounted on the anemometer and the motion parameters like position, velocity, and attitude were measured along with wind velocity in real-time. The attitude measurements were used to rotate the measured wind vectors from the sensor's frame of reference to the tracker's frame of reference. Furthermore, velocity measurements from the tracker were subtracted from the wind measurements to compensate for any motion in the anemometer readings.

To obtain the wind flow map, the anemometer was placed at discrete locations on dense serpentine trajectories at different heights, and the compensated wind velocities were recorded with 3D position vectors in the global (fan) frame of reference. At each location, the wind flow was recorded for at least 20 s at an update rate of 100 Hz. For each location, both steady-state flow and turbulent component of the wind flow were computed using this recorded data.

5.1. Wind map generation

As mentioned before, the helicopter dynamics are significantly affected by the external wind flow pattern generated by the cruising vessel. As it is not possible to measure wind velocity at every point in space around the helicopter, the wind flow is approximated using a parametrized model based on a finite number of measurements. As shown in (12) the localized wind flow in the rotor hub's frame of reference is assumed to be composed two components: steady-state (with subscript L) and turbulent (with subscript T) and modelled as a Gaussian process. The (mean) steady-state flow component, being predictable, is modeled using 12 parameters linear model whereas the turbulent component, being stochastic in nature, has been modelled as

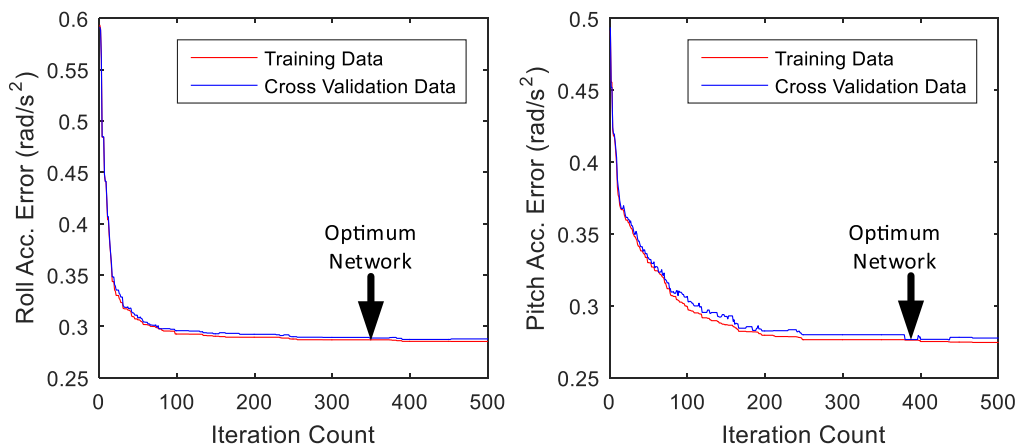


Fig. 6. Mean absolute error versus iteration count for PSO-NN.

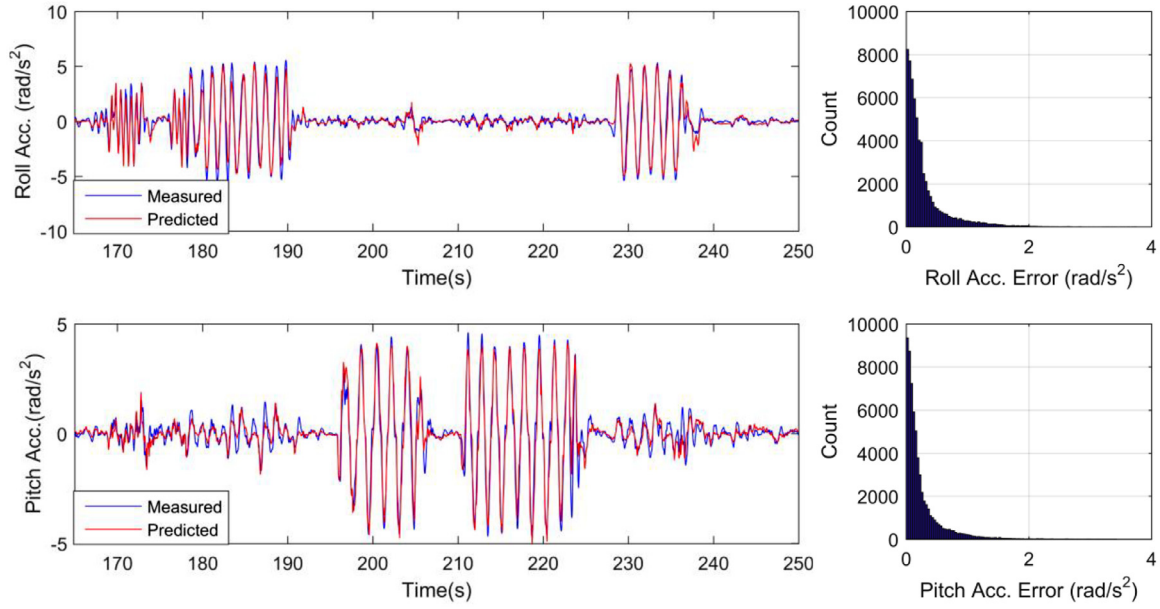


Fig. 7. PSO-NN prediction results for pitch and roll accelerations and prediction error distribution.

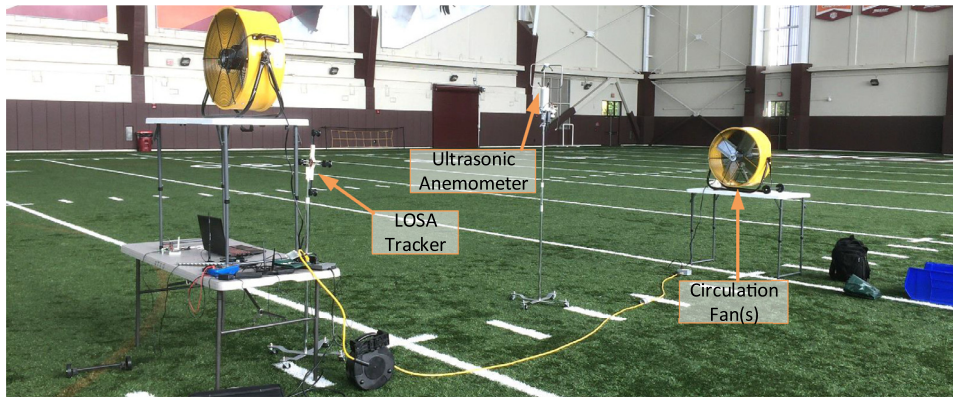


Fig. 8. Indoor wind flow mapping experiment setup.

a random variable with Gaussian distribution:

$$\begin{bmatrix} u_x \\ u_y \\ u_z \end{bmatrix}_{wh} = \left\{ \begin{bmatrix} a_x & b_x & c_x \\ a_y & b_y & c_y \\ a_z & b_z & c_z \end{bmatrix} \begin{bmatrix} x \\ y \\ z \end{bmatrix} + \begin{bmatrix} d_x \\ d_y \\ d_z \end{bmatrix} \right\}_L + \begin{bmatrix} u_x \\ u_y \\ u_z \end{bmatrix}_T ; \begin{bmatrix} x \\ y \\ z \end{bmatrix} = \begin{bmatrix} r_b c\psi \\ r_b s\psi \\ z \end{bmatrix} \quad (12)$$

Here u_{wh} is the wind velocity vector at a position vector $[x, y, z]^T$ with respect to the rotor hub in helicopter's frame of reference and $s\psi$ and $c\psi$ represent sine and cosines of the rotor position angle ψ respectively. To obtain the steady-state wind flow, for each location of the data recorded, a 12 parameter linear model (12) was fitted on the wind measurements within a volume of $1.3 \text{ m} \times 1.3 \text{ m} \times 0.6 \text{ m}$ (equivalent to helicopter's size) using the least square method. In the model (12), the vector $[d_x, d_y, d_z]^T$ represents the mean steady-state flow vector in the volume. The steady-state wind flow parameters were then interpolated to a 3D grid of 5 cm size using bilinear interpolation to generate a 3D wind map for the experiment.

To assess the accuracy of the model (12) the interpolated steady-state flow parameters were compared against the interpolated measured flow. Fig. 9A shows the spatial distribution of the error in modeling the measured wind flow with respect to the measured flow. As shown in the histogram (Fig. 9B) of the model deviations, represented as a percentage of the wind flow of 7.24 m/s at the source (circulation fans), most of the modeling error falls in 3–11% error bracket. High

error zones are visible on the corner of the modeled volume is due to the boundary effects of the interpolation process.

The turbulent component of the wind map was characterized by the standard deviation of the wind measurements after removing the steady-state component. The turbulence intensity was computed as the norm of the standard deviations of the 3-axis wind velocity measurements after subtracting the steady-state component (from the linear model) within the sample volume of $1.3 \text{ m} \times 1.3 \text{ m} \times 0.6 \text{ m}$. Similar to the steady-state flow, the turbulence map was generated by interpolating the turbulence intensity at a 3D grid of 5 cm.

Fig. 10 shows the final wind flow map generated by the experimental fans setup (Fig. 8). Here, the arrow field represents 3D steady-state wind flow field and the color represents the wind turbulence content of the wind flow in the form of standard deviation of the local wind speed. This turbulence data was used to map the helicopter's moment residuals to wind conditions for the calibration of the proposed system.

5.2. System calibration

To determine correlation between the helicopter's dynamics and wind turbulence, another indoor experiment was performed where the proposed system was flown in the region with the airflow modeled. As described in the Eqs. (8) and (10) local wind conditions directly affect

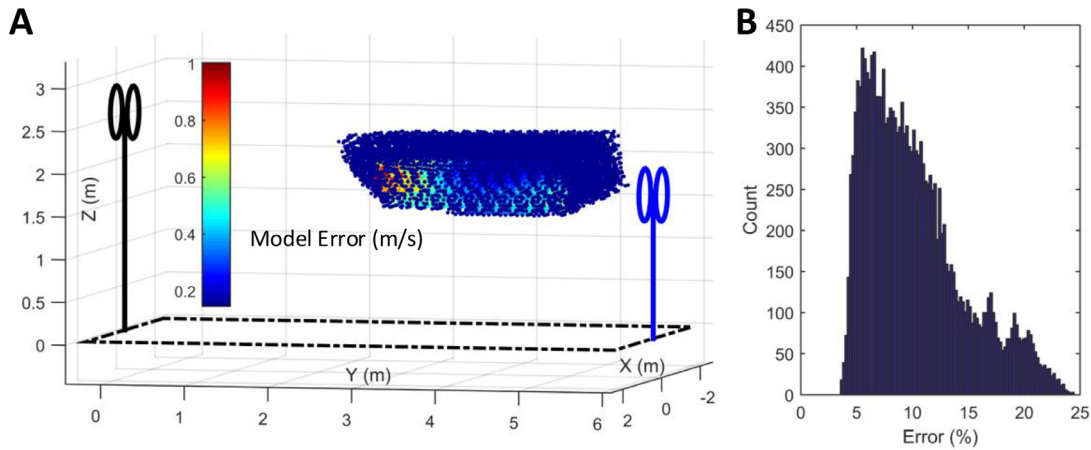


Fig. 9. Validation of steady-state wind model: A) Spatial distribution of modeling error, B) Histogram distribution of model error as a percentage of input wind.

helicopter dynamics. Wind turbulence, which is stochastic in nature, results in stochastic dynamics of the helicopter. Thus, similar to the turbulence intensity, the effects of wind turbulence on the helicopter are obtained from the standard deviation of the angular acceleration residuals obtained from the trained PSO-NNs.

During the calibration experiment, the helicopter was gently maneuvered between the two wind circulation fans as shown in Fig. 8. The LOSA motion tracker [26] was retrofitted onto the helicopter's fuselage for tracking the position and attitude of the helicopter. Since the same tracker was used for the wind mapping experiment, the helicopter motion and wind conditions were measured in the same frame of reference and hence can be compared directly. The angular acceleration estimates along the pitch and roll axes were converted from the helicopter's frame of reference to the tracker's (wind) frame of reference using attitude estimates obtained from the tracker. Then, for all the points on the helicopter trajectory, the norm of the local standard deviation of angular acceleration residuals (within a sample volume of $1.3\text{ m} \times 1.3\text{ m} \times 0.6\text{ m}$) was computed. The local standard deviations

of angular acceleration residuals were then interpolated over the test volume at a 3D grid of 5 cm and compared to the turbulence map. Fig. 11 shows the spatial distribution of the angular acceleration residual deviation (subfigure A) and wind turbulence (subfigure B), in the form of 3D slice plots on planes $X = 0\text{ m}$, $Y = 2.8\text{ m}$ and $Z = 1.8\text{ m}$.

For further analysis, the quantities from the two spatial distributions (shown in Fig. 11), were plotted and compared with each other (Fig. 12). Despite a high level of noise in the data, a positive correlation is clearly visible in the two quantities. As shown in (8), the moment exerted by the air wakes is proportional to the instantaneous wind conditions (turbulence). Hence, after assuming a linear relationship, the scaling factor coefficient between the angular acceleration residuals and wind turbulence was estimated using linear curve fitting. Due to the high levels of noise, RANSAC [31] optimization was used to fit a linear relationship between the two quantities. Fig. 12 shows the RANSAC inliers (in brown) and the linear fit line overlaid on the data points. The linear scaling coefficient for the angular acceleration residuals was obtained from the slope of the linear fit and was estimated

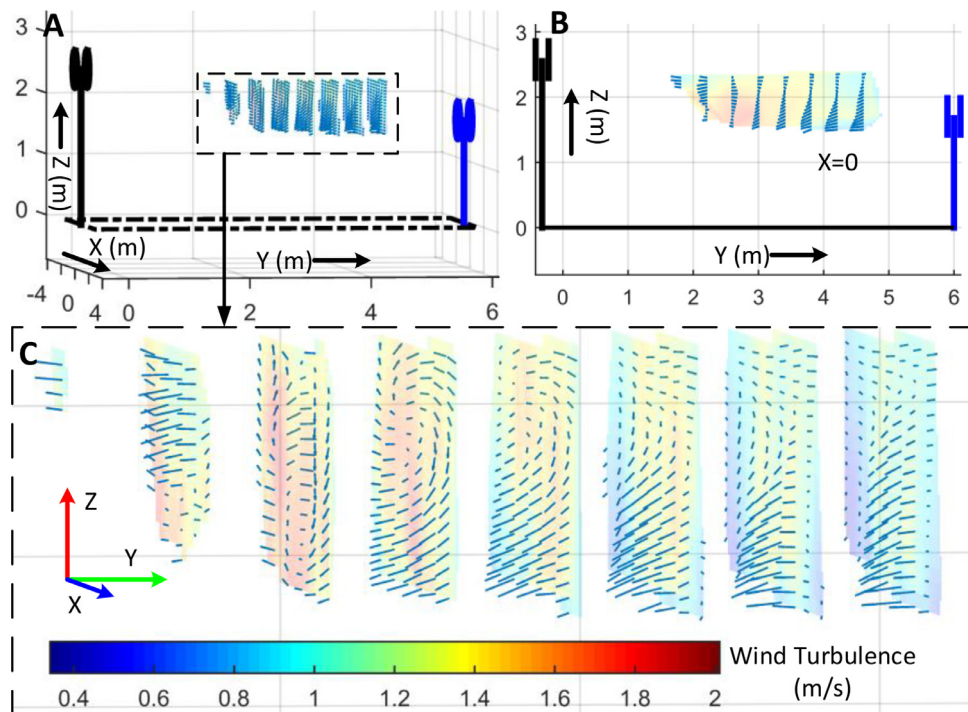


Fig. 10. Indoor wind flow map: (A) 3D steady-state wind flow with turbulence map; (B) Sectional view of the 3D flow field at plane $X = 0$; (C) Zoomed-in flow field.

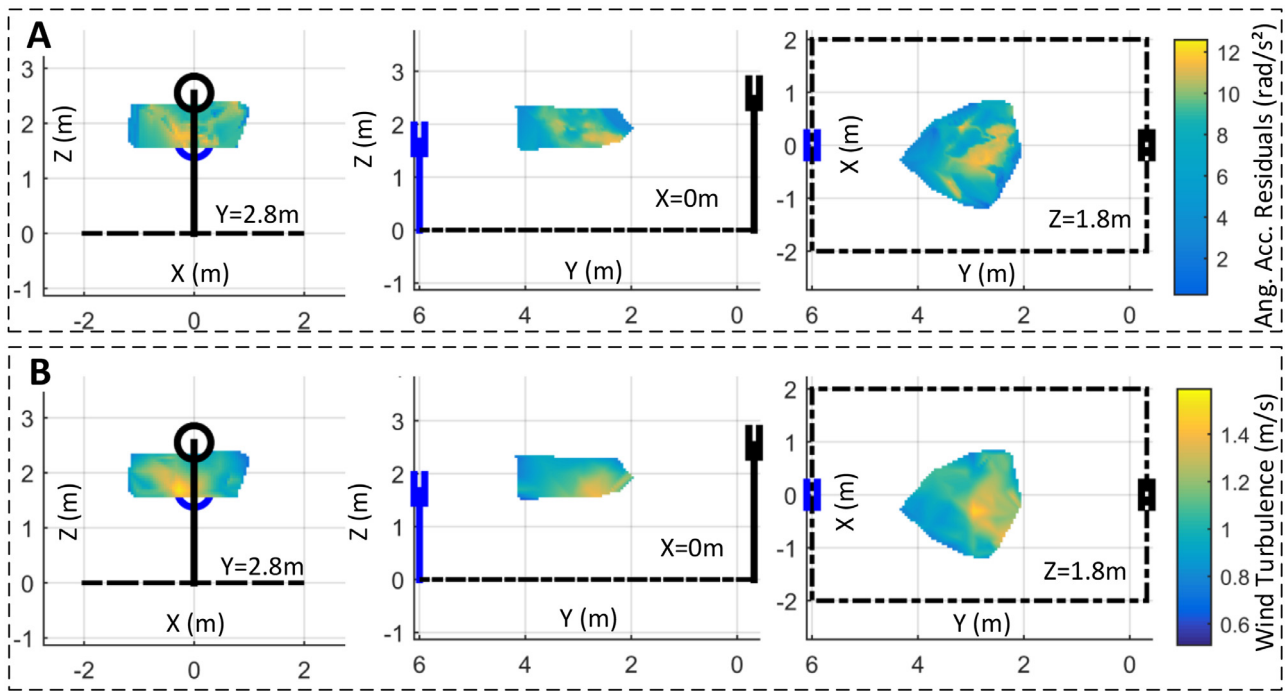


Fig. 11. Helicopter response to wind turbulence, (A) Local (standard) deviation of the angular acceleration residuals; (B) Wind turbulence map.

to be 0.021 m-s/rad. The offset arising from the linear model for the wind turbulence measurements is primarily result of sampling in a finite volume due to the sensing range limitation of the motion tracking device. As this paper focuses on estimations of relative distribution of the ship air wakes, the linear offset has been ignored while estimating wind turbulence from angular acceleration residuals.

6. Outdoor system testing and comparison with CFD results

The air wake intensity derived from the dynamics of the helicopter arising from interaction with air wakes is then plotted on a trajectory of the helicopter relative to the ship. The YP676 is equipped with an anemometer array to help the craft master to maintain near-constant relative wind conditions. Fig. 13 shows the telemetry system operating over the flight deck of a modified YP676 craft.

To map the ship air wakes generated by YP676 naval training vessel, an RC helicopter with the proposed instrumentation system was flown in the lee of the vessel at near constant altitude during flight ops conducted in the Chesapeake Bay. During experiments, the craft-master (of

the YP676) maintained a fixed relative wind speed of 6 knots (~ 3 m/s) with the help of vertically mounted acoustic anemometer array in the bow of the ship. The wind turbulence intensity was estimated from the localized standard deviation angular rate residuals and plotted on the trajectory of helicopter relative to the ship, then compared against CFD results for qualitative comparison and analysis.

CFD simulations were performed at USNA's advanced computing facility in Annapolis using Cobalt™ (a commercial parallel processing CFD software) on an unstructured tetrahedral grid of nearly 20 million tetrahedrons [3,16,17]. The USNA CFD simulation study used Monotone Integrated Large Eddy Simulation (MILES), a laminar, time accurate flow model, to simulate 30 s of wind flow field generated by a YP676 model against a head wind of 7 knots (3.6 m/s). In contrast to the definition used by the authors for ship air wake, the USNA study characterizes the ship air wakes as reduction in steady-state flow content computed as the norm of the time-averaged wind velocity vectors in the simulated flow field. While defined differently, the USNA study correlate well with the experimentation using the proposed system. Assuming equidistribution of kinetic energy throughout the simulated

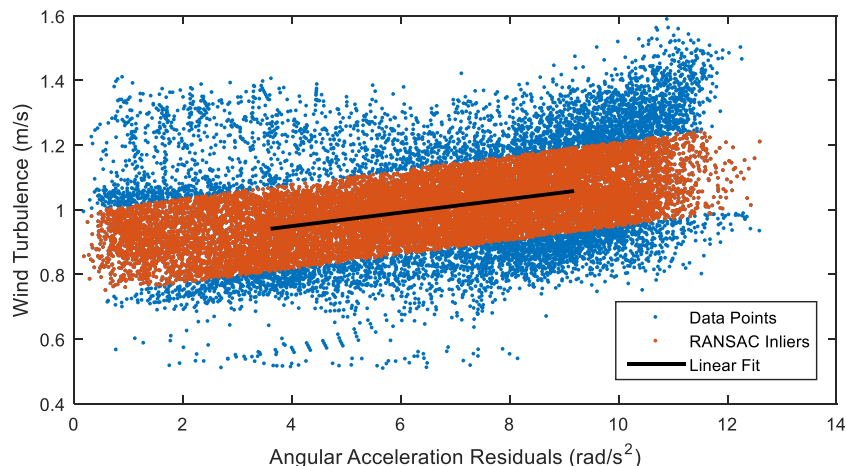


Fig. 12. Calibration of angular acceleration residuals for estimation of wind turbulence.

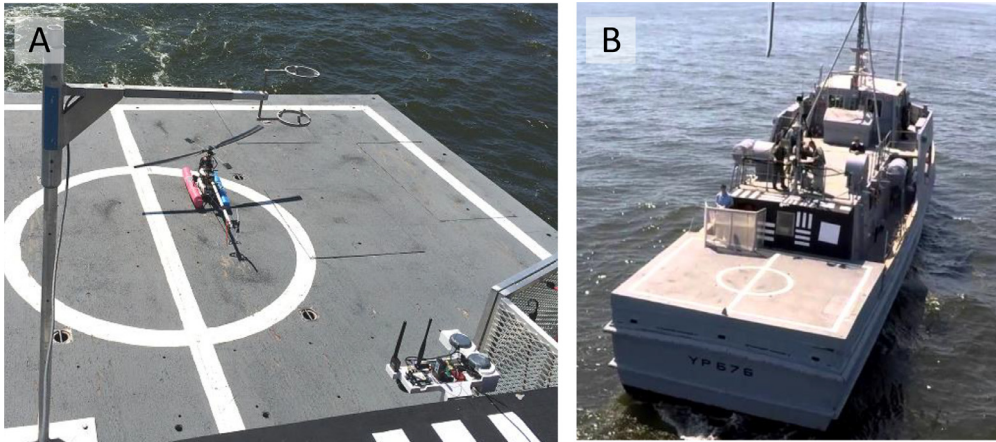


Fig. 13. Outdoor testing: (A) Telemetry system operating from YP676 flight deck (B) YP676 as seen from the RC helicopter.

volume, the regions with higher turbulence are expected to have relatively lower values for the norm of mean flow velocity vectors. Similarly, the regions with lower turbulence are expected to have higher values for the norm of mean flow velocity vectors (closer to the input head wind speed). For experimental data processing, the proposed system treats the norm of the standard deviation of the wind velocity vector (obtained from helicopter's angular acceleration residuals) as the ship air wake (turbulence) intensity. Thus the two datasets can be compared.

In Fig. 14A, simulated air wake pattern obtained in one of the previous studies [3] has been presented, where the color represents the turbulence intensity represented as of the norm of time averaged wind velocity vectors. The red color represents pure steady-state flow whereas blue color represents turbulent nature of the flow field. Fig. 14B shows the experimentally ship air wake pattern on a helicopter trajectory determined from the calibrated local standard deviation of angular acceleration residuals.

Although, the output from the proposed system and the CFD study represent different quantities, both physical quantities vary spatially with the change in local wind turbulence in an inverse manner. Due to the inaccessibility to the raw CFD data, the turbulence intensity computations, as defined in the presented study, cannot be computed for point-to-point comparison with the experimental data. However, a qualitative comparison is still possible from the two distributions. For qualitative analysis of the air wake patterns, the experimentally

obtained turbulence distribution was interpolated (using nearest neighbor interpolation followed by low pass filtering) over the area enclosed within the helicopter trajectory to generate a ship air wake map. Fig. 15 shows a comparison between the ship air wake patterns obtained from the CFD analysis and the proposed method.

Fig. 15A shows a cropped section simulated air wake pattern (presented in Fig. 14A) to compare against the experimentally obtained air wake map (Fig. 15B). A high air wake zone is visible between 5 m and 10 m in the aft of the test vessel. In addition, both maps show decay in air wake intensity with distance from the flight deck of the vessel. As described previously, contrasting definitions of wind turbulence in both studies yield different metrics, displaying an inverse relationship, yet with the same units of wind speed.

The experimentally obtained ship air wake map showed a good spatial correlation with the results obtained using CFD analysis. Fig. 15C shows a point-to-point comparison of the two air-wake maps with linear lift (using least squares method) plotted in red. Both maps show a negative correlation, as expected, (with Pearson correlation coefficient of -0.6450) with the slope of linear fit being -0.9292 . A less than perfect correlation between the distributions in some regions, especially in the farther regions from the vessel, can be attributed to the fact that the helicopter spent little time there in the presented study. Prolonged presence of the helicopter in a particular region would improve the accuracy of the air wake estimates.

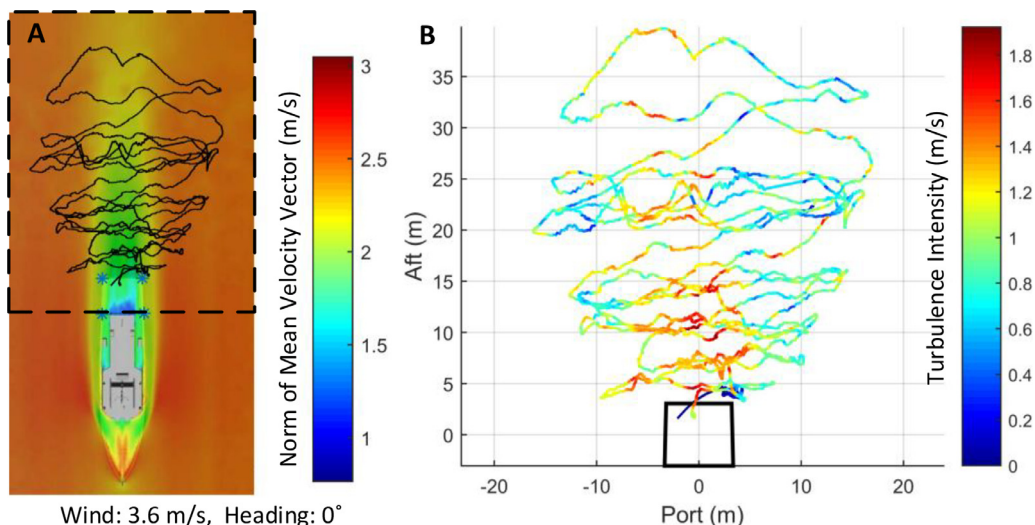


Fig. 14. Ship air wake distribution: (A) CFD model simulation results with experimental trajectory overlaid; (B) Experimentally determined turbulence distribution.

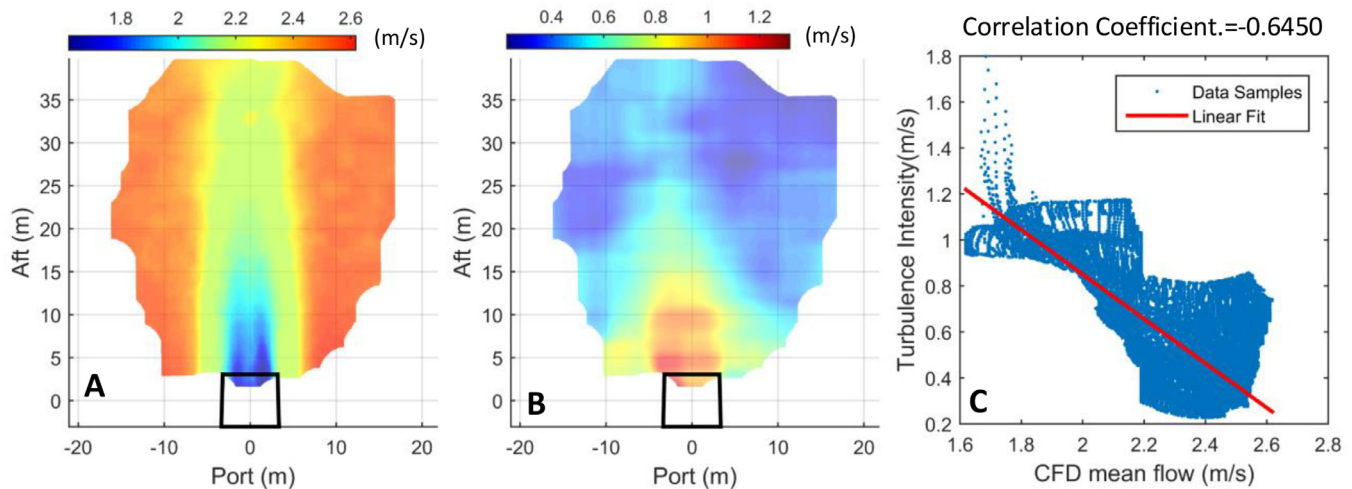


Fig. 15. Turbulence map comparison: (A) CFD mean flow simulation results; (B) Experimental ship air wake map (C) Turbulence cross-correlation.

7. Conclusion and discussions

This paper proposed a new sensing platform capable of quantizing and mapping wind turbulence patterns in large, open spaces where conventional instrumentation cannot be used. Being air borne, the proposed system not only increases the range of wind turbulence sensing, but also gives an absolutely safe and low cost means to map ship air wake patterns for naval vessels. The system was able to generate turbulence patterns during both indoor and outdoor experiments with good accuracy and correlation to CFD simulated turbulence patterns. By enabling the measurement of ship air wake effects experienced by the actual helicopters during ship board operations, the proposed system offers a low cost platform for the testing of control strategies for autonomous operations of helicopters in turbulent environments for both military and civilian applications.

System limitations and future work: The system currently relies on the rotational impact of wind turbulence on the helicopter to characterize air wakes. By including the helicopter's linear drift in the system model, the steady-state flow component of the wind pattern can also be estimated using the proposed system. In addition, neural networks represent a black-box type modelling technique of a system that is susceptible to error if the input data differ too much from the training dataset. An analytical dynamic modelling (of the helicopter) based framework is under active development, which will use all measured helicopter states (including linear motion) to provide a better characterization of the ship air wakes.

Acknowledgment

This research was partially funded by the Office of Naval Research. Program Officer is Mr. John Kinzer (Code 351). The authors are thankful to USNA and YP676 crew for their assistance in data collection. The authors would also like to acknowledge the assistance from Mr. Lester Karlín from the VT athletics department for his help in facilitating indoor flight experiments.

References

- [1] NAVAIR, Helicopter operating procedures for air-capable ships NATOPS manual, 2003. doi:NAVAIR 00-08T-122.
- [2] Guedes MJM, da MA, Vieira C, Martins ER, Moraes L. Brazilian navy air wake program. AIAA model. simul. technol. conf. Minneapolis, Minnesota 2012. p. 1–8. <http://dx.doi.org/10.2514/6.2012-4791>.
- [3] Snyder MR, Kang HS, Brownell CJ, Luznik L, Mikosovic DS, Burks JS, Wilkinson CH. USA ship air wake program overview. 29th AIAA appl. aerodyn. conf. Honolulu, Hawaii 2011. p. 1–12. <http://dx.doi.org/10.2514/6.2011-3153>.
- [4] Ferrier B, Duncan J, Nelson J, Carico D, Ludwig D, Deck C. Further validation of simulated dynamic interface testing limits computer based training, 2010.
- [5] Polisky S, Imber R, Czerwicz R, Ghee T. A computational and experimental determination of the air flow around the landing deck of a US navy destroyer (DDG): Part II. 37th AIAA fluid dyn. conf. exhib. Miami, Florida 2007. p. 1–12. <http://dx.doi.org/10.2514/6.2005-4958>.
- [6] Lee D, Horn J, Sezer-Uzol N, Long L. Simulation of pilot control activity during helicopter shipboard operations. AIAA atmos. flight mech. conf. exhib., american institute of aeronautics and astronautics 2003. <http://dx.doi.org/10.2514/6.2003-5306>.
- [7] Lee D, Sezer-Uzol N, Horn JF, Long LN. Simulation of helicopter shipboard launch and recovery with time-accurate airwakes. AHS 53th annu. forum am. helicopter soc. 2003. p. 448–61. <http://dx.doi.org/10.2514/1.6786>.
- [8] Ngo TD, Sultan C. Model predictive control for helicopter shipboard operations in the ship airwakes. J Guid Control Dyn 2016;39:574–89. <http://dx.doi.org/10.2514/1.G001243>.
- [9] Roper DM, Owen I, Padfield GD, Hodge SJ. Integrating CFD and piloted simulation to quantify ship-helicopter operating limits. Aeronaut J 2006;110:419–28.
- [10] Silva MJ, Wadcock AJ, Yamauchi GK, Long KR. Wind tunnel investigation of the aerodynamic interactions between helicopters and tiltrotors in a shipboard environment. Am. helicopter soc. 4th decenn. spec. conf. aeromechanics. 2004.
- [11] Kääriä CH, Wang Y, Padfield GD, Forrest JS, Owen I. Aerodynamic loading characteristics of a model-scale helicopter in a ship's airwake. J Aircr 2012;49:1271–8. <http://dx.doi.org/10.2514/1.C031535>.
- [12] Bardera-Mora R, Barcala-Montejano MA, Rodríguez-Sevillano A, de Diego GG, de Sotto MR. A spectral analysis of laser doppler anemometry turbulent flow measurements in a ship air wake. Proc. inst. mech. eng. part G J. aerosp. eng. 2015. p. 1–12. <http://dx.doi.org/10.1177/0954410015573972>.
- [13] Wadcock AJ, Yamauchi GK, Heineck JT, Silva MJ, Long KR. PIV measurements of the wake of a tandem-rotor helicopter in proximity to a ship. Am Helicopter Soc Aeromechanics Spec Forum 2004:1–23.
- [14] Allotta B, Pugi L, Massai T, Boni E, Guidi F, Montagni M. Design and calibration of an innovative ultrasonic, arduino based anemometer. Conf. Proc. - 2017 17th IEEE int. conf. environ. electr. eng. 2017 1st IEEE ind. commer. power syst. eur. IEEEIC / I CPS Eur. 2017. 2017. doi:10.1109/IEEEIC.2017.7977450.
- [15] Snyder MR, Kang HS, Brownell CJ, Burks JS. Validation of ship air wake simulations and investigation of ship air wake impact on rotary wing aircraft. Am Soc Nav Eng Launch Recover Symp 2012:18.
- [16] Snyder MR, Kang HS, Burks JS. Comparison of experimental and computational ship air wakes for a naval research vessel. Proc. 30th AIAA appl. aerodyn. conf. 2012. p. 1–25. <http://dx.doi.org/10.2514/6.2013-959>.
- [17] Snyder MR, Kumar A, Ben-Tzvi P, Kang HS. Validation of computational ship air wakes for a naval research vessel. Proc. 51st AIAA aerosp. sci. meet. 2013. p. 1–25. <http://dx.doi.org/10.2514/6.2013-959>.
- [18] Mallon CJ, Muthig BJ, Gamagedara K, Patil K, Friedman C, Lee T, Snyder MR. Measurements of ship air wake using airborne anemometers. 55th AIAA aerosp. sci. meet. 2017. p. 1–12. <http://dx.doi.org/10.2514/6.2017-0252>.
- [19] J.D. Metzger, Measurement of ship air wake impact on a remotely piloted aerial vehicle, 2012.
- [20] Kumar A, Ben-tzvi P. Extraction of impact of wind turbulence on RC helicopters using machine learning. ASME int. des. eng. tech. conf. Charlotte, North Carolina. 2016. p. 1–7.
- [21] Snyder MR, Kumar A, Ben-Tzvi P. Off ship measurement of ship air wakes using instrumented unmanned aerial vehicles. AIAA appl. aerodyn. conf. 2014. p. 1–9. <http://dx.doi.org/10.2514/6.2014-3100>.
- [22] Kumar A, Ben-Tzvi P, Saab W, Snyder MR. Wireless telemetry system for real-time estimation of ship air wakes with UAVs. Mechatronics 2016;36:18–26. <http://dx.doi.org/10.1016/j.mechatronics.2016.03.010>.
- [23] Kumar A, Ben-Tzvi P, Snyder MR. UAV-based wireless telemetry system for the estimation of ship air wake patterns. ASME int. des. eng. tech. conf. comput. inf.

- eng. conf. Boston, Massachusetts, USA 2015. p. 1–7. <http://dx.doi.org/10.1115/DETC2015-46656>.
- [24] Kumar A, Ben-Tzvi P, Snyder MR, Saab W. Instrumentation system for ship air wake measurement. ROSE 2013 - 2013 IEEE int. symp. robot. sensors environ. proc. 2013. p. 118–23. <http://dx.doi.org/10.1109/ROSE.2013.6698427>.
- [25] Padfield GD. helicopter flight dynamics: the theory and application of flying qualities and simulation modelling. 2nd ed. Oxford UK: Blackwell Publishing; 2007. <http://dx.doi.org/10.2514/2.4396>.
- [26] Kumar A, Ben-Tzvi P. Spatial object tracking system based on linear optical sensor arrays. IEEE Sens J 2016;16:7933–40. <http://dx.doi.org/10.1109/JSEN.2016.2607120>.
- [27] Bishop CM. Pattern recognition and machine learning. New York: Springer-Verlag; 2006. <http://dx.doi.org/10.1117/1.2819119>.
- [28] Clerc M, Kennedy J. The particle swarm-explosion, stability, and convergence in a multidimensional complex space. IEEE Trans Evol Comput 2002;6:58–73. <http://dx.doi.org/10.1109/4235.985692>.
- [29] Malik J, Mishra R, Singh I. PSO-ANN approach for estimating drilling induced damage in cfrp laminates. Adv Prod Eng Manag APEM 2011;6:95–104.
- [30] Young RM. Company Ultrasonic Anemometer - Model 81000, (n.d.). <http://www.youngusa.com/products/6/3.html> (accessed September 16, 2016).
- [31] Fischler Martin A, Bolles RC. Random sample consensus: a paradigm for model fitting with applications to image analysis and automated cartography. Commun ACM 1981;24:381–95.